

Cell-cell communication as underlying principle governing color pattern formation in teleost fishes

Received: 31 October 2025

Accepted: 3 February 2026

Published online: 18 February 2026

 Check for updates

Marleen Klann¹, Saori Miura¹, Shu-Hua Lee², Stefano Davide Vianello², Robert Ross³, Masakatsu Watanabe^{4,10}, Emma Gairin¹, Yipeng Liang⁵, Harrison W. Hutto⁵, Braedan M. McCluskey⁵, Marcela Herrera¹, Lila Solnica-Krezel⁶, Laurence Besseau^{7,8}, Simone Pigolotti³, David M. Parichy^{5,11}✉, Masato Kinoshita^{9,11}✉ & Vincent Laudet^{1,2,7,11}✉

The diverse pigmentation patterns of animals are crucial for predation avoidance and behavioral display. This diversity arises from interactions among distinct pigment cell types, yet mechanisms generating pattern variation across teleost fishes remain incompletely understood. In zebrafish, Turing models have been proposed to explain stripe patterns, but it is unclear if they apply to other fishes. Here, we investigate the *Snowflake* mutant of the anemonefish *Amphiprion ocellaris*, which displays enlarged white bars with irregular boundaries. Using genome-wide association mapping and targeted sequencing, we identify a missense mutation (E42K) in *gja5b*, encoding the gap junction protein Connexin 41.8. CRISPR/Cas9-mediated genome editing recapitulates the *Snowflake* phenotype, while pharmacological inhibition of gap junctions phenocopies the boundary defects, supporting a causal role for impaired intercellular communication. Expression analyses reveal that, unlike zebrafish, anemonefish *gja5b* is predominantly expressed in iridophores. With functional in vitro assays we demonstrate that the E42K mutation acts as a dominant negative, strongly reducing gap junctional coupling. Introducing the same mutation in zebrafish reveals context-dependent effects on pigment patterning. Taken together our findings highlighting gap junction-mediated communication as a conserved but flexible mechanism controlling pigment boundary positioning and pattern diversification.

Pigment patterns are among the most striking traits in animals, playing a role in predator avoidance, communication, and thermoregulation¹. Understanding how pigment patterns form and diversify is therefore crucial in elucidating the processes underlying morphological organization. In ectothermic vertebrates, these patterns emerge from the spatial arrangement of chromatophores – specialized pigment cells (such as black melanophores and yellow/orange xanthophores) or light reflecting cells (like iridescent/white iridophores) in the skin.

Studies of zebrafish (*Danio rerio*, Cyprinidae) reveal how self-organizing interactions of chromatophores are coordinated by morphogenetic behaviors, specification and differentiation to generate and maintain an organized pattern (reviewed in ref. 2). Theoretical and empirical investigations in this model species have shown that the dynamics of stripe formation can be described with Turing-type reaction-diffusion models, in which short-range activation and long-range inhibition between pigment cells, in particular via gap junctions,

A full list of affiliations appears at the end of the paper. ✉ e-mail: dparichy@virginia.edu; kinoshita.masato.4e@kyoto-u.ac.jp; vincent.laudet@oist.jp

are central in establishing patterns^{3,4}. This is illustrated by stripe formation failure in spotted *leopard* and *luchs* mutants. These harbor mutations in *gap junction gene 5b* (*gja5b*; *connexin 41.8*) and *gja4* (*connexin 39.4*), respectively, encoding Connexins that function in gap junctions of melanophores and xanthophores^{5,6}. It is not known if similar principles explain the wide range of patterns across other teleost fish lineages^{4,7,8}. For instance, the distantly related anemonefish *Amphiprion ocellaris* (Pomacentridae; Fig. 1A), has a simple and robust color pattern: an orange body adorned with three vertical black bordered white bars, which appear sequentially from head to tail during metamorphosis⁹. This color pattern remains stable as the fish grows, suggesting that it is established during development by interactions between chromatophores operating within a positional framework⁹. This may potentially combine reaction-diffusion-type mechanisms with positional cues. Three types of pigment cells, or chromatophores,

make up the color pattern in *A. ocellaris* (1) the orange body color mainly comprise yellow pigment cells (xanthophores) with some dispersed black pigment cells (melanophores) (2) the white bars mainly consist of white pigment cells (iridophores) with few scattered black pigment cells, and (3) black outlines of the white bar contain a dense array of black pigment cells (melanophores)^{10,11}.

Here, making use of one of many spontaneously arisen variants of anemonefish bred for tropical fish hobbyists¹², we focused on the *Snowflake* mutant (Fig. 1B), which exhibits jagged boundaries between colored bars that suggest defects in chromatophore communication. We show that a point mutation in *gja5b* underlies the *Snowflake* phenotype, thereby demonstrating a role for this locus and gap junction interactions in anemonefish and zebrafish, which last shared a common ancestor more than 200 million years ago¹³. Nevertheless, anemonefish *gja5b* is expressed by iridophores, unlike zebrafish *gja5b*

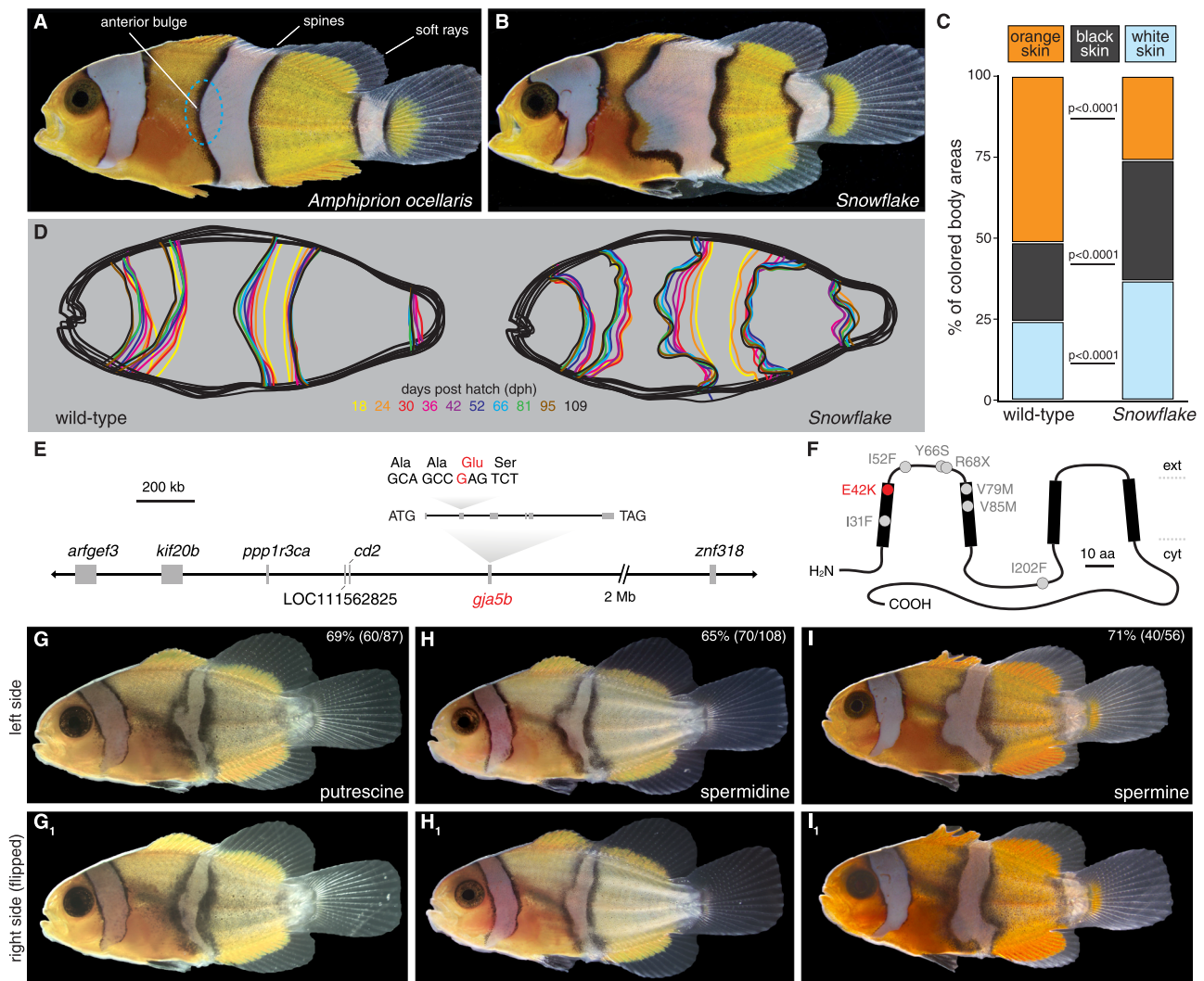


Fig. 1 | *Snowflake* phenotype, underlying gene candidates, and pharmacological gap junction inhibition. **A** The wild-type *Amphiprion ocellaris* color pattern comprises three vertical white bars with black edges on an orange body. The trunk bar shows an anterior bulge (blue oval). The dorsal fin spines and rays are indicated. **B** The *Snowflake* mutant color pattern is characterized by increased white areas with undulating, thicker outlines. **C** Comparison of colored body areas between wild-type and *Snowflake*, with increased white and black skin in *Snowflake* (Two-sided overall MANOVA, $F_{3,54} = 78$, overall and all individual comparisons, $p < 0.0001$; $n = 23$ wild-type, 35 *Snowflake*). Source data are provided as a Source Data file. **D** During color pattern development the *Snowflake* phenotype deviates from the wild-type from the beginning with broader white areas that develop

increasingly jagged boundaries as development proceeds (dph, days post-hatching). **E** GWAS analysis revealed 7 potential candidate genes, of which only one, *gja5b*, exhibited a coding sequence variant fully associated with the *Snowflake* phenotype. **F** *Gja5b* showing transmembrane domains (thick line segments), E42K mutation of *Snowflake* and previously identified variants of zebrafish. (ext, extracellular face; cyt, cytosolic face). **G–I** When pre-metamorphic wild-type larvae were treated (reared in drug-infused water) with polyamine gap junction inhibitors, putrescine (G/G₁), spermidine (H/H₁), and spermine (I/I₁), fish developed irregular bars, similar to *Snowflake*. These abnormal pigment patterns arose regardless of the number of positively charged amino groups (putrescine +2, spermidine +3, spermine +4), suggesting the blocking mechanism is highly sensitive.

(which is expressed in xanthophores and melanophores), and the *Snowflake* phenotype is qualitatively different from that of an identical mutation in zebrafish. Lastly, by engineering a parallel cellular context in zebrafish and modulating gap junctional communication of pigment cells with iridophores, we find defects in pattern formation consistent with those of *Snowflake*. Our findings illustrate how the same molecular players used in different contexts contribute to phenotype diversification and underscore cell-cell communication as a key principle in pattern formation.

Results

Snowflake mutants are defective for pattern boundary positioning

In comparison to wild-type *A. ocellaris* (Fig. 1A), the color pattern of *Snowflake* (Fig. 1B) differs in three ways (1) white areas are increased (Fig. 1C) (2) more melanophores occur within black edges (Fig. 1C), and (3) bar outlines are uneven (Fig. 1D). Expansion of white bar areas was evident dorsally, where the numbers of white spines and soft rays of the dorsal fin were significantly increased in two-month juvenile *Snowflake* fish compared to wild-type fish (Fig. S1A). Total areas covered by white bars were also significantly increased, comprising ~50% of the total body in *Snowflake* as compared to only ~30% in wild-type (Fig. 1C).

In *Snowflake* individuals the black boundary between orange and white areas is uneven and jagged. The black edge in wild-type *A. ocellaris* is relatively straight with no bends under 150°, except for the anterior bulge on the body bar (circled area in Fig. 1A) which is on average 149 degrees ($\pm 5.6^\circ$). On the contrary, the black edge of *Snowflake* juveniles possesses several bends between 120–150° (Fig. S1B). Moreover, even bends between 70–120° are readily observed in *Snowflakes* (Fig. S1B), but never in wild-type. Another way to assess the unevenness of the black edge is to calculate the total distance from dorsal to ventral edges (see Methods). In *Snowflake* the black edge is considerably longer (Fig. S1C) than in wild-type, due to its jaggedness that becomes more pronounced as the color pattern matures (Fig. 1D).

Black edges in *Snowflake* are also thicker. The dominating body color of wild-type juveniles (2 months) is orange (on average 63%), followed by white (on average 30%) and black (on average 7%) (Fig. 1C). By contrast, *Snowflake* juveniles have nearly twice the black body area (on average 13%). This increased black area mainly results from increased thickness of the edges due to the incorporation of more melanophores (on average 10.45 ± 1.36 melanophores in *Snowflake* vs. 6.67 ± 0.77 melanophores in wild-type).

Interestingly, every *Snowflake* fish has a unique appearance – the ways by which the black edge is curved and uneven differs between individuals. Yet each fish shows a very high degree of bilateral symmetry (Fig. S1D–F).

Anemonefish exhibit two distinct color patterns during development. Larval coloration was dominated by two horizontal stripes of black melanophores. At this stage, wild-type and *Snowflake* fish were phenotypically indistinguishable (Fig. S1G). Upon metamorphosis, when the adult color pattern started appearing, the *Snowflake* pattern became characterized by broader white areas (yellow lines in Fig. 1D). The mutant pattern was fully established after 2–3 months, with only minor alterations during later growth, indicating a defect in pattern formation rather than maintenance.

A connexin gene, *gja5b*, is mutated in *Snowflake*

The *Snowflake* mutation of *A. ocellaris* is assumed to have appeared only once in aquaculture (1999 Tropical Marine Centre, UK) and then spread in the pet shop trade. A *Snowflake* pair produces about two-thirds *Snowflake* offspring (48/76; 63.2%) and one-third wild-type offspring (28/76; 36.8%), suggesting a dominant mutation having an early lethal phenotype when homozygous.

To identify the gene (or genes) underlying the *Snowflake* phenotype, we used next generation sequencing of whole genomes from 20 phenotypically wild-type and 20 phenotypically *Snowflake* siblings derived from a backcross using the same wild-type female (Fig. S2A). Single nucleotide variants (SNVs) were found in 5 of the 24 chromosomes: chromosomes 2 (24 SNVs), 16 (7219 SNVs), 17 (2 SNVs), 20 (2 SNVs), and 22 (2 SNVs) (Fig. S3). The largest cluster of SNVs, a total of 7219 representing 99.59%, was located towards the end of chromosome 16 (Chr 16: 27,125,997 bp – 34,594,892 bp), including 1828 variants with a maximal heterozygosity score of 40, indicating heterozygosity in all *Snowflake* samples but homozygosity in all wild-type samples (see Methods). We therefore focused on chromosome 16 because of the largest number of high scoring candidate SNVs and mapped the variant types for each of the 1828 SNVs with heterozygosity score of 40 (Fig. S4). 10 missense variants, belonging to 7 genes, were identified and scrutinized further (Fig. 1E). Among these, *gap junction protein alpha 5b* (*gja5b*) stood out because it is the anemonefish orthologue of zebrafish *leopard* (Fig. S2B), encoding gap junction protein Connexin 41.8 (Cx41.8)⁵, a major actor in the Turing-like pigmentation patterning system in zebrafish¹⁴.

Using Sanger sequencing on *Snowflake* fish from different aquaria retail stores, we ruled out all genes other than *gja5b* (Table S1) as plausible candidates. In *Snowflake gja5b*, we identified a 124 G > A transition mutation, leading to a Glu42Lys (E42K) amino acid substitution towards the extracellular side of the first transmembrane domain of the Connexin (Fig. 1F). We observed that all *Snowflake* mutants surviving past the first three days of larval life were heterozygous, while homozygous *Snowflake* mutants developed and hatched but died rapidly after without any clear phenotype (Fig. S1G). Consistent with a critical role of *gja5b* during normal early larval development, stage-wise transcriptomic data revealed an upsurge in its expression at 2 days post-hatching (stage 2 in Fig. S2C).

To further test the correspondence of *Snowflake* and *gja5b*, we used two independent approaches. First, given that the candidate gene encoded a gap junction protein, we predicted that pharmacological inhibition of gap junctional communication in wild-type fish should lead to defects resembling those of *Snowflake*. We found that each of three polyamines (putrescine, spermidine, and spermine) known to inhibit gap junction communication¹⁵ resulted in uneven bar outlines strikingly similar to those of *Snowflake* in genotypically wild-type fish (Fig. 1G–I). By contrast, treatment of *Snowflake* individuals with polyamine did not alter the mutant phenotype (Fig. S2D), as anticipated if the mutation already blocks gap junctional communication. Second, to gain genetic confirmation we employed CRISPR/Cas9 methods to induce mutations because we reasoned that due to the dominant *Snowflake* phenotype knockdown methods might not necessarily mimic the phenotype. We predicted that if the *Snowflake* phenotype is due entirely to the observed mutation, rather than regulatory or other variants, then a corresponding mutation generated independently in an otherwise wild-type background should phenocopy *Snowflake*. Accordingly, we used CRISPR/Cas9 homology directed repair (HDR) to replace exon 4 of *gja5b* in wild-type fish with a homologous sequence having an E42K mutation (Fig. S2E,F). In GO fish, 14% of 102 surviving juveniles exhibited abnormal color patterns reminiscent of *Snowflake* (Fig. 2A), with individual variation and asymmetries (distinct from the normal bilateral symmetry) as expected given genetic mosaicism (compare Figs. 2A, B, two sides of the same fish). We additionally targeted the E42 codon directly by CRISPR/Cas9, to induce a spectrum of mutations by non-homologous end joining. Survival rates at hatching (27/131, 21%) and for juveniles (13/131, 10%) were reduced in comparison to injections replacing the entire exon (189/387, 49% at hatching and 102/387, 26% for juveniles), consistent with a subset of allelic mutations leading to early lethality, as observed in *Snowflake* homozygotes. Nevertheless, all 13 surviving juvenile fish displayed *Snowflake*-like phenotypes, with most fish showing an effect on all three

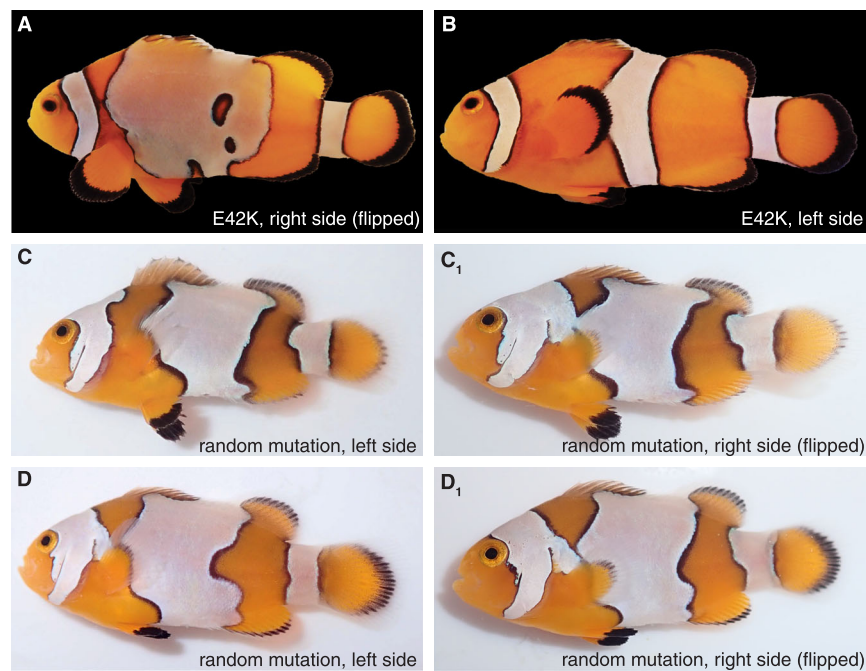


Fig. 2 | CRISPR/Cas9 genome editing replicates the *Snowflake* phenotype. **A** and **B** Targeting wild-type *gja5b* with an E42K substitution resulted in *Snowflake*-like phenotypes (**A**, severe bar disturbance; **B**, opposite side of the same mosaic

individual with wild-type pattern). **C/C₁** and **D/D₁** CRISPR/Cas9 mutations induced by NHEJ in the vicinity of E42 also led to phenotypes similar to *Snowflake* in G0 fish, displaying moderate bilateral symmetry.

white bars (Fig. 2C, D). Together these findings indicate that *Snowflake* results from an E42K substitution in *gja5b*, the gene encoding gap junction protein Connexin 41.8.

Cell-cell communication governs color pattern formation in anemonefish

To further understand the function of gap junctional communication during color patterning in anemonefish, we assessed the expression of *gja5b* across the three major pigment cell types in the fish through bulkRNAseq of scales of each of the three colors, namely orange, black and white. Due to the absence of black-only scales in *A. ocellaris*, we complemented our dataset with scales from a widely available mutant *A. ocellaris* strain whose body color is black instead of orange (*Black A. ocellaris*¹²), as well as the sister species *A. percula* that has scales representing each of the colors (Fig. 3A). As expected, samples from each color contained transcripts for markers genes of their corresponding pigment cell types (Fig. 3A). Crucially, however, our analysis revealed high levels of *gja5b* transcript in white scales, enriched in iridophores (Fig. 3A). *gja5b* transcript was found only at low levels in orange scales (enriched in xanthophores) and black scales (enriched in melanophores). The finding that *gja5b* is predominantly expressed in iridophores was surprising as *gja5b* of zebrafish is expressed primarily in xanthophores and melanophores (Fig. S5A). To confirm the spatial expression pattern of *gja5b*, we produced transgenic fish harboring GFP driven by *gja5b* promoter using the transposon system (Fig. S5B). In 18 of 19 (95%) G0 mosaic fish, we detected extensive expression of EGFP in white bars (Fig. 3B). Even though most of the *gja5b* expression domains are evident in white bar areas, we found minor reporter expression sites in orange skin (74%) (Fig. S5C), which is populated by xanthophores and melanophores. Additional minor expressions were detected in fin rays (53%) (Fig. S5C), lens (47%) (Fig. S5C), vasculature (32%) (Fig. S5C) and scales (32%). Therefore, we cannot formally exclude broader expression, and we do not claim iridophore-specific expression. Nevertheless, these findings suggest that, in anemonefish, *gja5b* primarily contributes to pigment patterning through its role in iridophores.

The heterozygous phenotype of E42K substitution raised the possibility of dominant negative activity, as inferred previously for some semi-dominant alleles of zebrafish¹⁶. We therefore assayed the function of E42K alleles in a *Xenopus* oocyte transjunctional current assay¹⁷. Injected wild-type *gja5b* cRNA allowed transjunctional currents, demonstrating that gap junctions were formed and electrical signals propagated (Fig. 3C). By contrast, E42K cRNA abolished current, indicating a failure in electrical signal propagation (Fig. 3C). Co-injection of equimolar E42K and wild-type cRNAs further indicated a strong dominant negative effect (Fig. 3C). We infer that the mutant protein most likely fails to permit gap-junctional dependent communication between cells sufficient for normal pattern formation in vivo.

In zebrafish, Gja5b forms heteromeric gap junctions with Gja4 (mutated in *luchs*¹⁸) and we therefore searched candidate partner connexins for anemonefish Gja5b. In *A. ocellaris* 42 gap junction genes could be identified (Fig. S6A). We screened expression of these gap junction genes in scales of the three different colors of wild-type fish, detecting 23 (Fig. S6A, highlighted). Most gap junction genes (18 out of 23) were expressed in two or more color-regions whereas *gja5a* and *gja5b* were expressed predominantly in the white area (Fig. S6B). Interestingly, *gja4a* was expressed in orange xanthophore-enriched tissue and black melanophore-enriched tissue consistent with the expression of its orthologue in zebrafish. In anemonefish, iridophores and xanthophores are not in direct contact¹⁰ and therefore gap junction formation is unlikely, but it is possible that Gja5b of iridophores forms gap junctions with Gja4a of melanophores. We therefore tested if three connexins consistently expressed across samples by xanthophores and melanophores (Gja2a, Gja4a, and Gjc2; Fig. S6B, asterisks, Fig. S6C) can form heterotypic gap junctions with Gja5b expressed predominantly by iridophores. Injection of cRNAs for each of the three connexins into *Xenopus* oocytes showed that all of them could form functional gap junctions on their own (Fig. 3D). We then performed assays using pairs of oocytes, one oocyte injected with Gja5b and the other oocyte with one of the three connexins to test if functional gap junctions can be formed. When Gja2a or Gja4a was injected into *Xenopus* oocytes, functional gap junctions were formed with Gja5b-

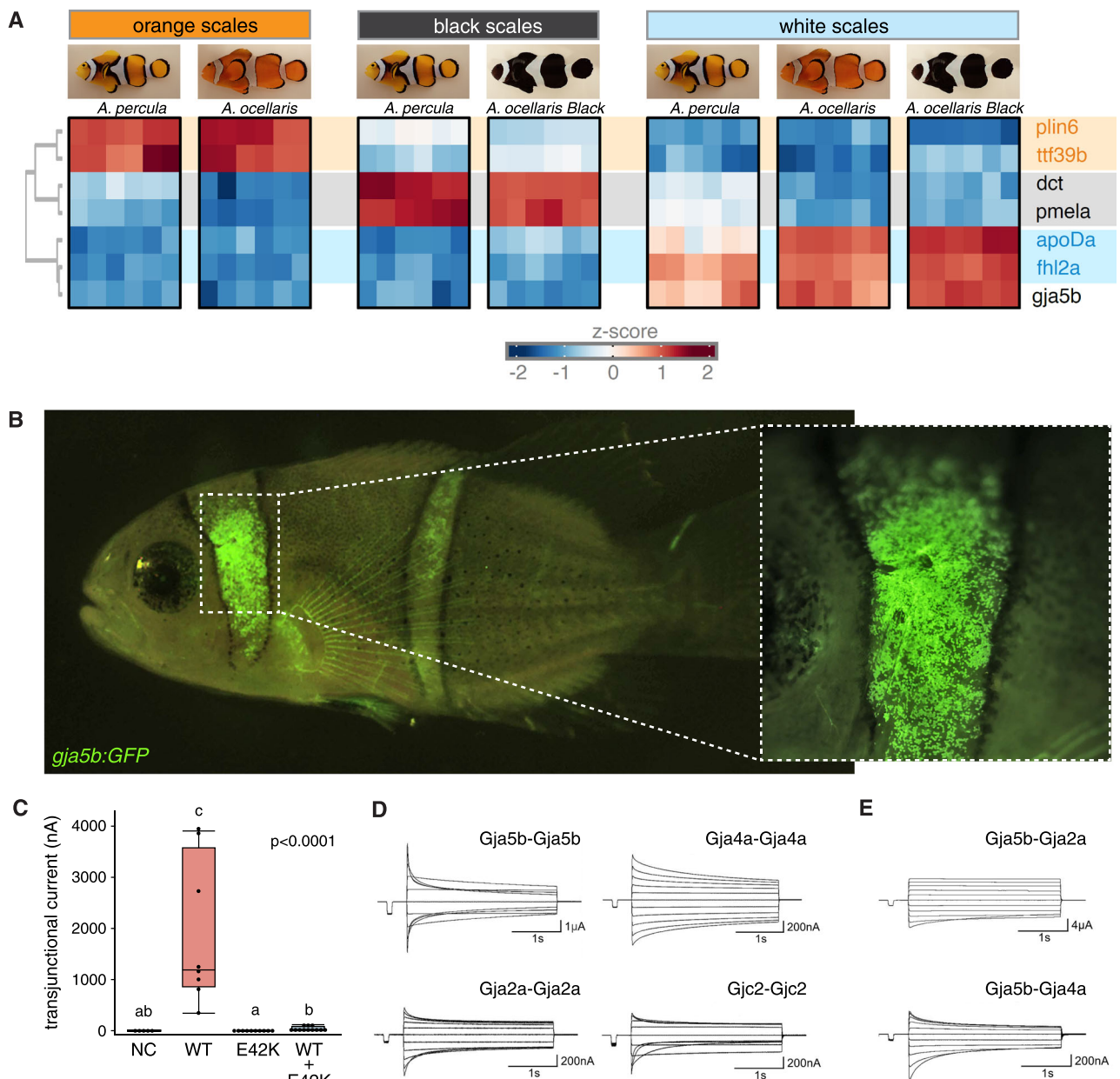


Fig. 3 | Anemonefish *gja5b* expression and transjunctional current assays.

A RNA-sequencing of scale samples enriched for orange xanthophores (marker genes: *plin 6* and *tt39b*), black melanophores (marker genes: *dct* and *pmela*) and white iridophores (marker genes: *apoDa* and *fhl2a*) revealed highest *gja5b* expression in association with iridophores. Scales were collected from wild-type *A. ocellaris*, *Black A. ocellaris* mutant and wild-type *A. percula* (the latter two fish were added to obtain samples of pure black color). The color scale corresponds to z-scored expression values (z-score = value in each sample – “mean across samples”, all divided by the gene expression standard deviation across samples). **B** The expression of *gja5b* was monitored by GFP. The GFP gene driven by *gja5b* promoter was introduced into 19 wild-type fish (for construct see Fig. S5B). Predominant GFP expression was found in white bar areas (18/19 individuals). **C–E** Transjunctional current assays in *Xenopus* oocytes were performed to test the formation and

functionality of gap junctions. **C** In comparison to transmitted current at -100mV for wild-type (WT) Gja5b, little to no current was transmitted by E42K-mutated *gja5b*, singly or in combination with wild-type. NC, no-construct control. Data are represented as box and whisker plots with boxes containing medians and extending from 25th percentile to 75th percentile (interquartile range) and whiskers extending to the last point within 1.5x interquartile range. Source data are provided as a Source Data file. (Two-sided Overall Kruskal-Wallis, χ^2 approximation=24.6, $p < 0.0001$; shared letters over groups indicate medians not significantly different from one another by *post hoc* Steel-Dwass comparisons.) **D** Homotypic gap junction of Gja5b, Gja2a, Gja4a, and Gjc2 are functionally active. **E** Heterotypic gap junctions between Gja5b and Gja2a and between Gja5b and Gja4a are functionally active.

injected oocytes ($n = 3$ for Gja2a, $n = 6$ for Gja4a; Fig. 3E). In contrast, heterotypic gap junctions formed between Gja5b and Gjc2 either failed to produce functional gap junctions or showed extremely low activity consistent with the absence of the ExxE domain at position 12–16 in its protein sequence ($n = 4$; Fig. S6D). Further experiments will be necessary to elucidate the partner or partners of Gja5b in melanophores (with Gja2a and Gja4a as potential candidates) and iridophores.

Iridophore-specific manipulation of *gja5b* disrupts pigment patterning in zebrafish

Expression of *gja5b* in white bars of *A. ocellaris* and its presumed function in iridophores contrasted with zebrafish, in which *gja5b* is expressed and required in melanophores and xanthophores. Zebrafish *gja5b* mutant alleles confer a range of spotted phenotypes with null alleles being recessive and homozygous viable^{5,18,19}. We identified a new

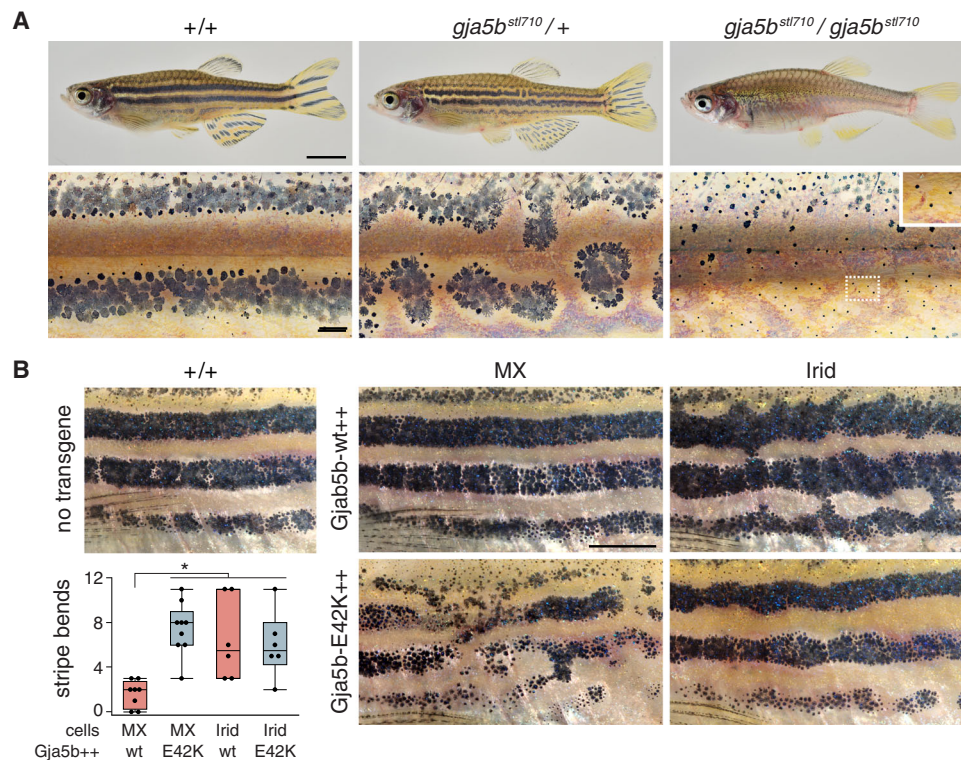


Fig. 4 | An E42K mutation in zebrafish and patterning consequences of gap junctional perturbation by misexpression. **A** Comparison of wild-type zebrafish and mutants heterozygous or homozygous for E42K mutant allele *gja5b^{stl710}*. For each transgene 6–9 F0 individuals were scored. Inset shows higher magnification of melanin in individual, dispersed melanophores of homozygous mutant. **B** The top left panel displays the wild-type appearance of zebrafish stripe without injected transgene. Overexpression of wild-type Gja5b (Gja5b-wt++) in melanophores and xanthophores (MX) did not result in a visible phenotype (8 individual injected fish, top middle) whereas overexpression of mutant Gja5b (Gja5b-E42K++) led to phenotypes similar to *leopard* mosaics (9 individual injected fish, bottom middle). By contrast wild-type Gja5b expressed by iridophores (Irid) resulted in

melanophores trespassing into interstripes (6 individual injected fish, top right), and expression of mutant Gja5b resulted in wandering stripe boundaries and expanded interstripe regions (6 individual injected fish, bottom right). The bottom left panel shows that pattern irregularities, assessed as bends in stripe boundaries, were significantly increased when iridophores expressed wild-type Gja5b ectopically, or when either set of chromatophores expressed E42K. Data are represented as box and whisker plots with boxes containing medians and extending from 25th percentile to 75th percentile (interquartile range) and whiskers extending to the last point within 1.5x interquartile range. Source data are provided as a Source Data file. (Two-sided ANOVA, $F_{3,25} = 8.10$, $p = 0.0006$, * indicates $p < 0.001$). Scale bars, 1 cm (in A, upper), 200 μm (in A, lower), 1 cm (in B).

ethylnitrosourea-induced allele in zebrafish, *gja5b^{stl710}*, which, by chance, presented the identical nucleotide change and amino acid substitution (E42K) as *Snowflake*, allowing a direct comparison of phenotypes between the two species (Fig. S7). Zebrafish *gja5b^{stl710}* exhibited a heterozygous phenotype of irregular stripes grading into spots and a homozygous viable phenotype of few widely dispersed melanophores associated with a failure to coalesce into stripes (Fig. 4A; Fig. S8A; movies S1, 2) and severe attenuation of electrical current flow (Fig. S8B). These findings show that, as in anemonefish, cell-cell communication via gap junctional coupling is essential for pattern formation, consistent with and building upon inferences of prior studies using zebrafish.

Given the correspondence between these mutations and their consequences for gap junctional communication, and considering the expression and presumed function of *gja5b* in iridophores of anemonefish, we hypothesized that gap junctions of zebrafish iridophores – in addition to those of melanophores and xanthophores – function in stripe formation. Indeed, single cell RNA-sequencing revealed that iridophores can express low levels of *gja5b* during adult stripe formation (Fig. S5A). If iridophores participate in gap junctional communication, we predicted that blockade of such communication should lead to pattern defects. We therefore mosaically expressed wild-type or dominant negative Gja5b^{E42K} in wild-type zebrafish using the promoter of *defbl1* which drives expression at high levels in iridophores but not melanophores or xanthophores²⁰. Overexpression of Gja5b^{WT} in iridophores led to melanophores trespassing into light

interstripes, whereas Gja5b^{E42K} led to expanded interstripes with irregular boundaries (Fig. 4B; Fig. S8C). These phenotypes were specific to iridophores, as overexpression of Gja5b^{WT} specifically in melanophores and xanthophores using a promoter derived from *mitfa*²¹ did not affect stripe borders whereas expression of Gja5b^{E42K} in these cells led to phenotypes resembling those of individuals chimeric for *leopard* mutations¹⁹ (Fig. 4B).

These results support a model in which all three major chromatophore classes are responsive to changes in gap junctional activities, with these activities contributing to the formation of the very diverse color patterns of teleost fish species as phylogenetically distant as zebrafish and anemonefish, emphasizing the importance of gap junction mediated communication in pigment patterning.

Boundary modeling reveals low tension and dynamic noise in shaping *Snowflake* phenotype

We turned to biophysical modeling to better understand the effect of the *Snowflake* mutation on white bar patterning. We implemented an approach based on the Edwards-Wilkinson model, which describes the dynamics of membranes and interfaces²². This approach assumes that the boundary separating color patches develops under the effect of random fluctuations and surface tension. In this context, the tension represents the effect of cell-cell interactions (such as those potentially mediated by gap junctions) that keep together cells of the same color type, thereby reducing roughness of the boundary. In contrast with models parameterized for very specific cellular behaviors of gene

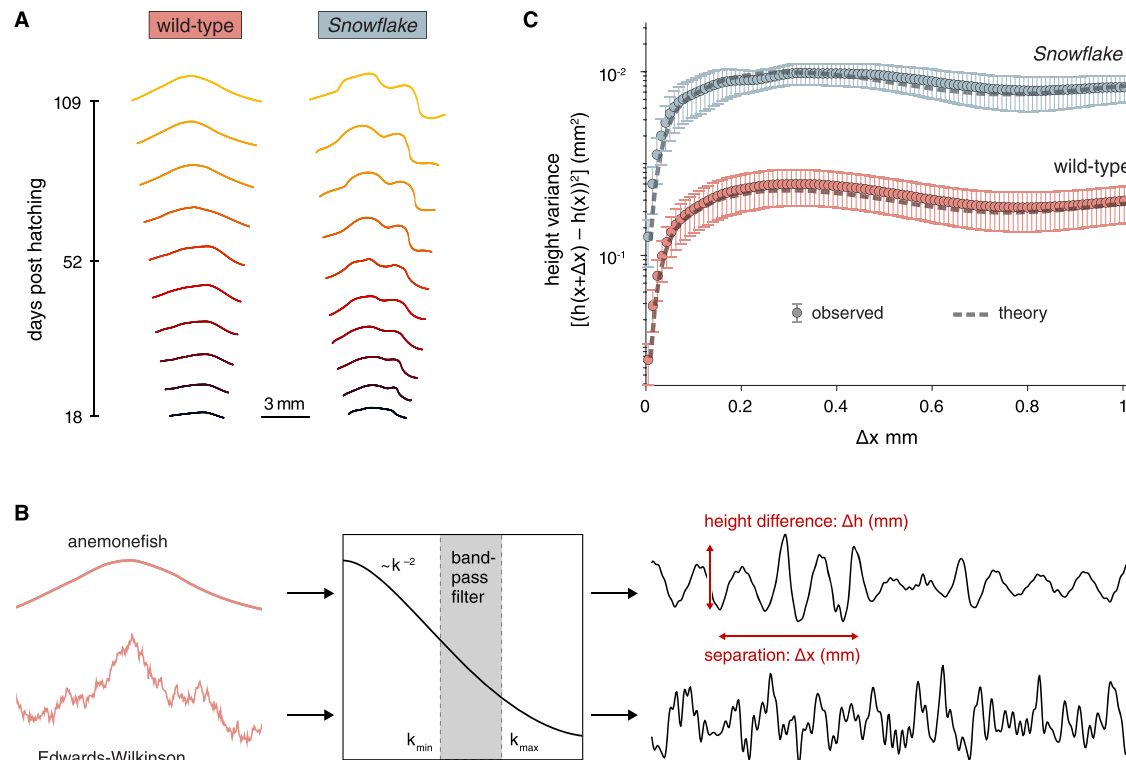


Fig. 5 | Boundary modeling in wild-type and *Snowflake* fish. **A** Examples of boundary shapes traced in developmental series of wild-type (WT) and *Snowflake* (SF). **B** Representation of selected modeling steps applied during Edwards-Wilkinson. **C** Theoretical prediction of the Edwards-Wilkinson model and actual

measurements (acquired for 10 individual fish per genotype) fitted very well. Data are represented as mean values \pm SEM. Source data are provided as a Source Data file.

activities²³, our approach does not require detailed mechanistic and experimental knowledge of cell-cell interactions or gene regulatory networks. It is therefore particularly appropriate for anemonefish, an emerging model organism for which our knowledge of the processes is still limited⁷.

To apply the model to anemonefish patterning, we traced boundary shapes of the trunk bar (both anterior and posterior individually) in developmental series of wild-type and *Snowflake* (Fig. 5A). We then applied a band-pass filter to the data to remove large scale fluctuations due to body shape and therefore not captured in the model, as well as small-scale fluctuations due to experimental error in measuring contours (Fig. 5B and Methods). Resulting estimates of boundary fluctuations in wild-type and *Snowflake* were in excellent agreement with the predictions of the Edwards-Wilkinson model (Fig. S9). In this comparison, the K ratio, representing the ratio between the intensity of random fluctuations and surface tension, was about one order of magnitude larger in *Snowflake* than in wild-type ($K = 0.0039 \pm 0.0001$ for WT anterior; $K = 0.00426 \pm 0.00005$ for WT posterior; $K = 0.082 \pm 0.005$ for SF anterior; $K = 0.13 \pm 0.01$ for SF posterior).

We used the model to predict boundary roughness quantified as the variance of the boundary height difference Δh between points on the line at a certain distance Δx (Fig. 5B and Methods). According to the model, the roughness increased approximately linearly with distances on the order of 0.2–0.3 mm, and then plateaued at an approximately constant value, which is dependent on the parameter K. This theoretical prediction agreed with the boundary roughness measured directly from experimental data, both for the anterior trunk bar boundary (Fig. 5C) as well as the posterior trunk bar boundary (Fig. S9E). Goodness-of-fit tests treating the Edwards-Wilkinson model as a null hypothesis showed no significant deviation between theory and data (reduced $\chi^2 < 1$; $p > 0.93$). We therefore conclude that, within

experimental uncertainty, the EW model provides a good description of observed variance in patterns across conditions. The comparison of observation and modelling supports that both the anterior and posterior boundaries of the trunk bar in *Snowflake* are rougher, as a combined effect of more intense fluctuations and reduced surface tension.

Discussion

In this study, we identified *gja5b* as the gene mutated in *Snowflake*, showing that a single amino acid change in the encoded connexin Cx41.8 disrupts pigment pattern formation in anemonefish. The *Snowflake* phenotype, with its uneven and curved bar outlines, emerges from a defect in boundary positioning during metamorphosis. Modeling revealed that these jagged contours likely reflect higher dynamic noise and/or reduced tension between color domains. While the precise geometry of the disrupted boundaries varies markedly between individuals, the two sides of each *Snowflake* fish remain strikingly similar (Fig. S1D–F). This combination of inter-individual variability and strong bilateral symmetry suggest that pattern formation is not dominated by stochastic cellular noise, but instead unfolds within a robust, organism-level framework that constrains left–right outcomes. We therefore infer that reduced intercellular tension relaxes local boundary constraints while preserving global developmental coordination, allowing individual-specific boundary shapes to emerge reproducibly within each animal. These considerations suggest the mutation disturbs how these cells communicate and in so doing determine their respective position. In wild-type fish, sharp boundaries likely rely on precise communication between iridophores and melanophores, a process compromised in *Snowflake* due to the *gja5b* mutation, resulting in rougher outlines and broader white areas. Interestingly, expressing the same mutant allele in zebrafish iridophores also caused boundary defects, highlighting a conserved role for

gap junction dependent interactions despite differences in cell-type specific expression of *gja5b* itself. Our data suggests that cell-cell communication is not only critical for shaping boundaries, but also for maintaining the normal chromatophore ratios during pattern formation, as shown by the broader white areas in *Snowflake*.

The roles of gap junctions in pigment patterning appear to be both widespread and highly adaptable across teleost fish. In our study, the E42K mutation in the connexin *gja5b* was shown to disturb pigment cell arrangement in both anemonefish and zebrafish, even though the gene is expressed in different chromatophore types between the two species. Studies on species as diverse as marble trout, chicken, and quail also highlighted the importance of *gja5* orthologues in color patterning^{24–26}. These findings indicate that connexins, especially *gja5* but likely others too, have been co-opted repeatedly for color pattern formation across distant teleost fish and in other vertebrates. What differs is not necessarily the function of the protein itself, but the context in which it was deployed: the pigment cell types, their spatial arrangement, and their interaction dynamics. This flexibility suggests that pigment pattern evolution can proceed not only through changes in gene expression or cell fate, but also by rewiring the communication channels between pigment cells. From this perspective, pigment patterns become not only a readout of cell identity, but also a dynamic product of tissue-level signaling. This kind of redeployment likely contributed to the vast diversity of pigment patterns observed in teleosts and other vertebrates. That such mechanisms rely on electrical and chemical coupling via gap junctions, a system also fundamental in heart, brain or fins, highlights the deep evolutionary plasticity of cellular communication in shaping several traits.

Beyond explaining the *Snowflake* phenotype, our results suggest a potential route by which macroevolutionary diversification of color patterns could occur. Gap junctions represent a modular and tunable mode of cell–cell communication: altering their expression level, cellular context, partner specificity, or biophysical properties can modify interaction strength without changing pigment cell identity. Such changes are well suited to generate quantitative variation in pattern geometry—such as boundary sharpness, bar width, or edge regularity—rather than complete pattern loss. This is consistent with the observation that many teleost lineages differ not in the presence or absence of stripes or bars, but in their spacing, curvature, continuity, and stability. In this framework, evolutionary changes affecting connexins or other components of gap junction networks could fine-tune self-organizing pigment cell interactions within a conserved positional scaffold, producing diverse pattern outcomes across species. Importantly, because gap junctions are reused across chromatophore types and developmental contexts, similar molecular changes can produce distinct pattern outcomes depending on cellular deployment. This flexibility offers a complementary route for color pattern evolution through modifications of intercellular communication and tissue-level biophysical properties, without altering pigment cell identity or number.

The *Snowflake* mutation, by altering *Gja5b* function, impaired pigment cell communication and effectively reduced pigment cell diffusion. As supported by our modeling, this disruption affected short-ranged cell coordination and transformed sharp bar boundaries into irregular expanded regions. Recent analysis of pattern formation of teleost fishes suggested that the blending of patterns generated by Turing patterning can generate diversity⁴ but our results suggest that another dimension should be added as positional cues or boundary information complement self-organizing processes. In anemonefish the number, position, and overall shape of white bar patterns are fixed during growth, a behavior not expected from classical Turing mechanisms, which typically scale with size, as observed in zebrafish. This stability and strong bilateral symmetry suggest that positional cues act early to define the global placement of bars. Within this positional framework, local self-organized interactions between

pigment cells, mediated by gap junction communication, are likely to contribute to shaping bar boundaries. Thus, rather than opposing reaction–diffusion models, our results support a composite mechanism in which positional information constrains global pattern layout, while self-organizing cell–cell interactions fine-tune boundary geometry in *A. ocellaris*. More broadly, our results showed that altering biophysical properties in the skin can generate strong pattern changes without modifying the pigment cell types or their gene expression. In other words, pattern diversity can emerge not only from which cell types are present, but also from how these cells are organized and interact within the tissue. This view is consistent with morphodynamic patterning models²⁷ where tissue-level dynamics and mechanical feedback shape pattern outcome. By modulating how information spreads between cells, gap junction networks could offer a versatile and evolvable means to shape pattern diversity. While their wiring and timing may vary between species, the underlying logic of using regulated cell-cell communication to organize pigment patterns seems largely conserved.

Methods

The research presented in this study complies with all relevant ethical regulations from the following institutions:

University of Virginia, Institutional Animal Care and Use Committee (ACUC) protocol (#4170) (zebrafish work).

Animal Experiment Section of OIST, protocol number ACUP-2023-0125 (most of the anemonefish work).

Kyoto University, protocol numbers #250192 (anemonefish genetic modifications) and #R7-45 (animal experiments).

The experiments using *Xenopus* were approved by Nagoya University and performed in accordance with institutional guidelines.

Phenotypic comparison during development

To obtain high-quality images to access the *Snowflake* phenotype, sibling fish (in total 23 wild-type and 35 *Snowflake*) were anesthetized with 100 mg/L MS222 (Sigma-Aldrich), placed in a petri dish and images of both sides were taken using a Discovery.V20 stereoscope (Zeiss) mounted with a AxioCam 208 color camera (Zeiss). Images of the same individual fish were taken successively, covering with every 1–2 days before 30 days post hatching, and being reduced to every 3–5 days before 60 days post hatching, while images were taken only every 7 days after 60 days post hatching. Adobe Photoshop 2025 was used to adjust brightness and to remove the background in images selected for representation in the main text and Supplementary Figs. and figures were assembled using Adobe Illustrator 2025. JMP Pro Statistical Software was employed for all statistical analyses. This software does not report exact *p*-values when less than 0.0001.

To quantify white area expansion the width of the body bar was measured by counting the number of dorsal fin spines and dorsal fin soft rays the bar encompassed (Fig. 1A). Additionally, white areas were calculated as follows: First, using ImageJ an outline was drawn manually around the entire body and the area was determined. Second, using ImageJ outlines were drawn manually around each of the three white bars and the areas were determined (Fig. S10A). Lastly, the percentage of white areas in relation to the total body area was calculated either individually for each bar or combined (total white area). The same procedures were followed to calculate the orange and the black area, respectively.

The bending angles of the black edge were calculated using ImageJ (Fig. S10B). Wild-type *A. ocellaris* have one bending angle of about 120–150°, which is sometimes referred to as the “bulge”. This is usually located on the anterior edge of the body bar, approximately on level with the midline.

The length of the black edge (body bar only) was calculated for both the anterior and posterior edge individually (Fig. S10C). First, a straight line was drawn to connect the dorsal and ventral points were

the black met the body outline. Next, a curved line was traced along the actual black edge. Both line values were put into relations – with a value of 1 indicating the shortest possible outcome.

All anemonefishes start as males and only change sex into females if they are put in a couple with another smaller male. Sex of the fish has not been considered, but it is likely that all fish analyzed were males.

SNV analysis

The genomes of 20 wild-type (WT) and 20 heterozygous *Snowflake* (SF) sibling fish were sequenced. DNA extraction was done using Promega ASI400 Maxwell RSC Blood DNA Kit (Promega) following the manufacturer's instructions with an added RNase step. Library preparation (NEBNext® Ultra™ II FS DNA Library Prep Kit for Illumina) and DNA Shotgun Sequencing (150 bp, pair ends) using NovaSeq 6000 S2 whole (NovaSeq 6000 S2 Reagent Kit v1.0, 300 cycles) was performed by the in-house sequencing center (OIST SQC, sample ID 137). Raw genomic data were processed using the Genome Analysis Toolkit (GATK4 v4.2.0) framework²⁸ following Altrabio's (www.altrabio.com) recommended pipeline. Briefly, quality of raw reads was assessed using FastQC v0.11.9 (<https://www.bioinformatics.babraham.ac.uk/projects/fastqc/>). Adapters, primers, low quality ends (Phred score <30), and reads shorter than 35 bp were removed with Trimmomatic v0.36²⁹ using the parameters ILLUMINACLIP:TruSeq3-PE.fa:2:30:10:2:true LEADING:3 TRAILING:3 SLIDINGWINDOW:4:15 MINLEN:36. Sample contamination was evaluated using FastQ Screen v0.14.0. The *A. ocellaris* reference genome³⁰ was indexed using Bowtie2 v2.4.4³¹ and reads were aligned using the bwa-mem2 v2.2.1³² algorithm. The resulting alignments were sorted, marked for duplicates, and indexed using Picard tools v2.22.1 (<https://github.com/broadinstitute/picard>). Next, the GATK HaplotypeCaller tool was used to call variants per-sample, including summarized evidence for non-variant sites (GVCF workflow). The variant-calling matrices of the different alignments were then imported into GenomicsDB using GATK GenomicsDBImport and all samples were jointly genotyped with GATK GenotypeGVCFs. Variants were filtered based on the following criteria: "QD2" = QD < 2.0, "SOR3" = SOR > 3.0, "FS60" = FS > 60.0, "MQ40" = MQ < 40.0, "MQRS125" = MQRankSum < -12.5, "RPRS8" = ReadPosRankSum < -8.0 for SNVs, and "QD2" = QD < 2.0, "SOR3" = SOR > 3.0, "FS200" = FS > 200.0, "RPRS20" = ReadPosRankSum < -20.0 for indels. This resulted in a raw genotype matrix counting 5,189,387 SNVs and 1,416,665 indels (83.8% and 90.5% of the SNVs and indels that passed filtering, respectively). Subsequently, to annotate the variants, the reference genome³⁰ was annotated using the *A. ocellaris* genome and annotations from Ensembl. Mapping of the coordinates between the two assemblies and transfer of the Ensembl annotations onto the reference assembly were performed using Liftoff v1.6.1³³ with the option -polish. The software SnpEff v5.0³⁴ was then used to predict the putative effect of all variants.

A candidate SNV should ideally display a heterozygous state in all *Snowflake* sample (SF) but be in a homozygous state in all wild-type samples (WT). Therefore, after annotating the variants, these were further filtered by adding the number of heterozygous SF and homozygous WT at each position, which created a metric called "heterozygosity score". Given the number of fish, the score ranged between 0 (anti-pattern of all-homozygous SF and all-heterozygous WT) and 40 (desired pattern of all-heterozygous SF and all-homozygous WT). Co-segregating SNVs in coding regions were defined as variants with a score greater than 35 and were considered further.

SNV confirmation

Sanger sequencing was employed to rule out genes that are not primarily causing the *Snowflake* phenotype. Fish from three *Snowflake* strains, purchased either in France, Taiwan, or Japan, were fin clipped. DNA was extracted employing the Promega ASI400 Maxwell RSC Blood DNA Kit following the manufacturer's instructions with an

added RNase step. PCRs were performed for each of the seven candidate genes (primers details in Table S2) using either KOD FX (TOYOBO) or Go Taq (Promega) PCR kits (PCR conditions in Table S3). PCR products were purified using Exo-CIP™ Rapid PCR Cleanup (NEB). An automated Capillary sequencer (Thermo Fisher 3500xl Capillary sequencer) in combination with the primers listed above and the BigDye Terminator v3.1 Cycle Sequencing Kit (Thermo Fisher) were used for direct Sanger sequencing.

For each gene between 10–20 wild-type and 10–20 *Snowflake* fish were tested (Table S1). A gene could be excluded, if either one of the following were true (1) a phenotypic *Snowflake* offspring exhibited a homozygous wildtype genotype for a specific gene, or (2) a phenotypic wildtype offspring had a heterozygous mutant genotype for a specific gene (and a homozygous mutant genotype for this gene was never observed).

Phylogenetic analysis

Sequences for all available *gj* genes for *Danio rerio* and *Amphiprion ocellaris* were downloaded from NCBI. Sequences for *gja5* were downloaded for three additional species: *Oryzias latipes*, *Gasterosteus aculeatus*, and *Takifugu rubripes*. Conserved regions for *Danio rerio* were acquired from Mikalsen and colleagues 2020³⁵ and all individual NCBI sequences were aligned and trimmed to those conserved regions in SeaView. A NJ phylogenetic tree was created using MAFFT v7 selecting JTT substitution model and Bootstrap resampling of 1000.

Pharmacological experiments

Five to eight pre-metamorphic larvae between 6–8dph (days post hatching) were placed into a 500 mL glass beaker and incubated with commercially available pharmacological active small molecules. The following small molecules were used in this study: 0.3–0.6 mM putrescine (putrescine dihydrochloride P5780, Sigma-Aldrich), 0.2–0.6 mM spermidine (spermidine S0266, Sigma-Aldrich), 0.3–0.6 mM spermine (spermine S4264, Sigma-Aldrich) and 50–300 nM PQ7 (gap junction enhancer PQ7 5.06216, Sigma-Aldrich). The larvae were raised following previously published protocols³⁶. Every day 20% of water was changed and replaced with seawater including corresponding small molecules in the desired concentration. Incubation time varied between 5–10 days. To end the experiment the concentration of small molecules was dramatically lowered. First, 80% of the drug infused water was replaced with normal sea water, adding the water in small increments over several hours. Second, the following day 50% of the water was replaced with normal sea water. Imaging of larvae started the next day, three days after the end of the experiment. The larvae were anesthetized with 100 mg/L MS222 (Sigma-Aldrich), placed in a petri dish and images of both sides were taken using a Discovery.V20 stereoscope (Zeiss) mounted with a Axiocam 208 color camera (Zeiss). Images of the same fish were taken successively, every 2–5 days until all three bars were formed. This work has been approved by the Animal Experiment Section of OIST, protocol number ACUP-2023-0125.

CRISPR/Cas9 mutagenesis

For amino acid substitution, homologous gene knock-in method using CRISPR/Cas9-nickase system was employed.

Construction of SF- plasmid donor (Fig. S2E). A 697 bp fragment-SF, which contained *gja5b* exon 4 including the E42K mutation and its flanking regions, was amplified by PCR. A fragment-L was amplified by the primers Ao-gja5-HAL-XhoI-F and Ao-gja5-SF-R with genomic DNA as template. A fragment-R was amplified by the primers Ao-gja5-mut-F and Ao-gja5-HAR-SpeI-R with genomic DNA as template. Then, a mixture of fragments L and R was used as template to amplify fragment-SF by PCR with primers Ao-gja5-HAL-XhoI-F and Ao-gja5-HAR-SpeI-R. As a result, fragment-SF contained an amino acid substitution from Glu

(GAG) to Lys (AAA) and 11 silent mutations in the coding region (small orange letters in Fig. S10D), which enabled the designated design of specific primers for the detection of gene substitution (“Ao-KI-check-R” in Table S2). The fragment-SF and p2BaitD-acta1_500 bp-mAG³⁷ were digested with Xho I and Spe I and ligated to generate SF-donor plasmid. The donor plasmid contained two invert-repeat of BaitD sequence with which the knock-in fragment is cut out by Cas9-nickase³⁷.

To confirm successful substitution, skin from a G0 individual was collected, with one sample taken from a normal white bar (CRISPR fish WT bar) and another sample taken from a *Snowflake* reminiscent white bar (CRISPR fish SF bar). DNA from the skin tissues was extracted using Proteinase K and phenol/Chloroform. The substituted sequence was confirmed by PCR (KI-check primers) and followed by Next-generation sequencing. The amplicon was sequenced with NextSeq 1000 and analyzed subsequently. The reference *Amphiprion ocellaris* genome assembly ASM2253959v1³⁰; as downloaded from NCBI) was indexed with the “build” function of bowtie2 v2.4.4 (RRID:SCR_016368³¹). Raw sequencing reads were then aligned to this genome, using bowtie2 with default parameters. The resulting.sam files were sorted and converted to.bam files, using functions “sort” and “fixmate” from SAMtools v1.18 (RRID:SCR_002105³⁸) with default parameters. The resulting files could be imported into the Integrative Genomics Viewer (IGV) Desktop Application (RRID:SCR_011793^{39,40}), therefore obtaining pileup plots. Base percentages at each position of the *gja5b* coding sequence (LOC11585045) were obtained directly from the application and visualized as an Excel table. The introduced donor plasmid will induce a replacement of the codon 42 from GAG to AAA, if successful. Sequencing results showed a 0% substitution rate for wild-type fish, while the CRISPR G0 fish displayed some level of substitution: 1% for the WT bar and 6% for the SF-bar (Fig. S2F). The rate of the silent mutations in the CRISPR fish SF-bar also reached 6%, suggesting this was the percentage of successfully achieved genomic edits.

Microinjection. A mixture of Ao-gja5-crRNA2 (40 ng/ml, Target seq: TACGGCAGCCGAGTCTTCGTGGG, PAM), BaitD-crRNA (40 ng/ml, Target seq: GATCTTCGGCTAGACTGCGAGG), tracrRNA (140 ng/ml, FASMAC), Cas9-nickase protein (D10A)(1000 ng/ml, FASMAC), and the donor plasmid (2.5 ng/ml) was microinjected into the cytoplasm of 1- or 2-cell stage fertilized eggs as described previously⁴¹. A total of 387 eggs were injected, raised in egg tumblers and then transferred to tanks after hatching (hatching survival rate 189/387, juvenile survival rate 102/387). Fin clips were cut after 2-3 months and the presence of induced mutations within *gja5b* was checked via PCR (see above).

Random *gja5b* mutagenesis. For the induction of random mutations in *gja5b*, a single guide RNA (sgRNA2), targeted the same sequence as Ao-gja5-crRNA2, was synthesized with CUGA gRNA synthesis kit (NIP-PON gene) following the manufacturer’s instructions. Then, the sgRNA2 (100 ng/ml) and Cas9 protein (500 ng/ml, FASMAC) were microinjected into 1-cell stage of fertilized eggs as described previously⁴¹. A total of 131 eggs were injected, raised in egg tumblers and then transferred to tanks after hatching (hatching survival rate 27/131, juvenile survival rate 13/131). To confirm successful mutagenesis, five scales from white bars showing a *Snowflake* phenotype were picked from five CRISPR/Cas9 G0 fish. As a control, five scales from a white bar of one non-treated fish were picked. Scales were incubated in 8 ml of 25 mM NaOH and 0.5 mM EDTA at 95 °C for 10 min. After neutralization by addition of 10 ml 40 mM Tris-HCl, pH8.0, the resulting solutions were used as template for PCR. PCR was performed using KOD-FX DNA polymerase (TOYOBO) with primers TruSeq-F and TrySeq-R. PCR products were purified with NucleoSpin Gel and PCR Clean-up (Macherey-Nagel) following instructions. Then, sequencing was performed with NextSeq 1000. From each individual, more than 32000 amplicon reads were obtained. In the white bar of the non-

treated fish, no mutated reads were observed, only wild-type sequences. On the contrary, white bar areas of the five CRISPR treated fish contained many types of mutations, including short in-frame deletions (less than 19 nucleotides). Those were particularly frequent representing 22–52% of all reads in these fish (Fig. S2G) and believed to mainly contribute to the *Snowflake*-like phenotype.

Visualization of *gja5b* expression pattern

gja5b expression pattern was visualized with green fluorescence using Tol2 transposon system. A GFP expression plasmid driven by *gja5b* promoter, pTol2-Aogja5bPro6KGFP (Fig. S5B) was generated. The upstream region (ca. 6.6 kb) from translation codon (ATG) of *gja5b* was amplified by PCR using PrimeStar GXL DNA polymerase (Takara Bio) and primers Ao-gja5bPro-F0 and Ao-gja5bPro-R1 (Table S2). The Tol2 trap vector, pT2AL200R150⁴², was digested with Xho I and BamHI to remove intrinsic sequence of EF1a-P and the intron. The PCR fragment and digestive of pT2AL200R150 were ligated using In-Fusion HD Cloning Kit (Takara Bio). Tol2 transposase mRNA was synthesized from pCS-TP⁴³ using an mMessage mMachine SP6 Kit (Ambion). The mixture of pTol2-Aogja5bPro6KGFP (5 ng/ml) and Tol2mRNA (50 ng/ml) was microinjected into fertilized wild-type eggs (see above). A total of 113 eggs were injected, raised in egg tumblers and then transferred to tanks after hatching (hatching survival rate 28/113, juvenile survival rate 18/113). GFP fluorescence was observed using a fluorescence stereomicroscope (SZX16, OLYMPUS) with GFP filter set (excitation: BP460-495, emission: BA510IF).

Stage-wise transcriptomics

RNA extraction and sequencing. 10–15 Larvae of all seven identified postembryonic stages⁴⁴ were euthanized in 100 mg/L MS222, imaged with an Axiocam 208 color (Zeiss) mounted on a Discovery.V20 stereoscope (Zeiss) and stored in RNAlater (Sigma-Aldrich). RNA was extracted using AS1340 Maxwell RSC simplyRNA Tissue Kit (Promega) following the manufactures instructions. Library preparation (NEBNext® Ultra™ II Directional RNA Library Prep Kit for Illumina) and RNA Sequencing with poly-A RNA Purification (strand-specific, 150 bp, pair ends) using NovaSeq 6000 S2 whole (NovaSeq 6000 S2 Reagent Kit v1.5, 300 cycles) was performed by the in-house sequencing center (OIST SQC, sample ID 382).

Analysis. The complete Rnotebooks use for the analysis of the stage-wise transcriptomic data, the counts matrix, the gene and sample metadata files, as well as other data to reproduce the analysis are available at Zenodo [10.5281/zenodo.16892159](https://doi.org/10.5281/zenodo.16892159); the pipeline is summarized below. Raw (demultiplexed) fastq files were quality-checked based on reports generated by using FastQC v0.11.9 (RRID:SCR_014583; <https://www.bioinformatics.babraham.ac.uk/projects/fastqc/>) with default parameters, before and after adapter trimming. Adapters were trimmed using Trimmomatic v0.39²⁹ with parameters ILLUMINACLIP:TruSeq3-PE-2.fa:2:30:10:8:keepBothReads LEADING:3 TRAILING:3 SLIDINGWINDOW:4:15 MINLEN:36. Trimmed reads were quantified at the transcript-level using the pseudo-aligner kallisto v0.46.2⁴⁵ against the *A. ocellaris* reference transcriptome. The average mapping rate was 64.03% of total reads. The counts data was processed as a DGEobject (edgeR package, RRID:SCR_012802⁴⁶⁻⁴⁸) and differences in library size were taken into account by obtaining counts per million (CPM) values to allow a comparable threshold to filter out of lowly expressed genes. Here, we only maintained genes for which at least 10 counts could be detected (arbitrary) in at least 10 samples (our smallest experimental unit being $n = 10$ per treatment). This corresponded to a threshold of 0.95 CPM based on the sample with lowest library size, resulting in a filtering out of 1755 out of 14949 genes (11.7%). Heatmap visualizations were computed on the filtered count data, taking into account library size differences and correcting against compositional bias through the Median of ratios method internal to

the DeSeq2 pipeline (DESeq2 package, RRID:SCR_015687⁴⁹). Counts were then further variance stabilized (DESeq2's varianceStabilizing-Transformation function). All heatmaps were plotted using the function Heatmap from the ComplexHeatmap package^{50,51} reporting z-scores ((counts - mean)/sample standard deviation; base R's "scale" function with default parameters).

Scale transcriptomics

Transcriptomic data sets from color-specific scale and skin samples were analyzed. Both data sets showed similar results, but skin samples, especially black skin, comprised other pigment cells and were less pure for single chromatophores. Therefore, we focused our analysis on transcriptomic data acquired from scales. Because the purity of black color was limiting, we added samples from the *Black A. ocellaris* mutant strain in which the orange body color is replaced with black.

Around 100 scales of each color were manually collected and transferred into sterile 2 mL microcentrifuge tubes filled with 750 μ L ice-cold Trizol (TRI Reagent; Merck/Sigma-Aldrich) containing three autoclaved stainless steel beads (EBL Biotechnology). Samples were disrupted and homogenized by mechanical agitation in a vibrating bead mill (TissueLyser II, Qiagen, RRID:SCR_018623; 3 min, 30 Hz, room temperature). Homogenized sample lysates were stored at -80°C before RNA extraction. On the day of extraction, sample lysates were thawed on ice and centrifuged 10 min in a tabletop microcentrifuge at 11000 $\times g$, 4°C . 750 μ L of each supernatant were loaded into a dedicated RNA filtering column (NucleoSpin[®] RNA Mini kit; Macherey-Nagel) and processed according to the manufacturer's recommendations. RNA amounts and quality were initially assessed with a NanoDrop spectrophotometer (Thermo Scientific[™]) and by agarose gel electrophoresis (2:1 intensity ratio of 28S:18S bands; 800 ng of sample per lane, 0.6% Agarose in TAE-buffer, 1 h, 50 V). Extracted RNA was stored at -80°C until sequencing.

Quality-control, library preparation and sequencing of extracted scale and skin RNA were performed by the High Throughput Genomics Core at Academia Sinica, Taipei. RNA-Seq libraries were generated from 1000 ng of total RNA (or lower for few samples for which this amount could not be reached) using the Illumina Stranded mRNA Prep mRNA Sample Preparation Kit with UDI indices (Illumina) according to manufacturer's instructions. Surplus PCR primers were removed using AMPure XP Bead-Based Reagent (Beckman Coulter Life Sciences). Final cDNA libraries were checked for quality and quantified using Qubit (ThermoFisher Scientific) and Fragment Analyzer for size profiling (Agilent), and concentration-normalized using KAPA Library Quantification Kit for Illumina Platforms (Roche). Sequencing was performed on an Illumina NextSeq2000 for paired-end 150 base format. Libraries were loaded in a P3 flow cell. The fastQ files were generated and demultiplexed using the Illumina bcl2fastq v2.20 pipeline. A median of 26–29 million paired-end reads per sample were obtained (expected output ceiling: 27–31 million reads/sample). Three samples, which had shown low qPCR amplification rates during library preparation, produced a lower data yield than other samples, despite equal pooling. A further sequencing round was thus run for these samples (on a P2 flowcell), producing an average of 15 million extra reads for each. The complete Rnotebooks use for the analysis of the scale and skin transcriptomic data, the counts matrix, the gene and sample metadata files, as well as other data to reproduce the analysis are available at Zenodo [10.5281/zenodo.1689215](https://zenodo.org/record/1689215); the pipeline is summarized below.

Pre-processing. Raw (demultiplexed) fastq files were quality-checked based on reports generated by using FastQC v0.12.0 (RRID:SCR_014583⁵²;) with default parameters, before and after adapter trimming. Adapters were trimmed using the function bbduk (RRID:SCR_016969) of BBTools v39.01 (RRID:SCR_016968; Bushnell B., <http://sourceforge.net/projects/bbmap/>) with ktrim=r, and k=23, qtrim=r, trimq=30, trimpolyg=40. Categories flagged by FastQC after

trimming ("warning" or "fail") were analyzed in detail and judged not to be prejudicial to further analysis.

Analysis. For scale transcriptomic data, trimmed reads were quantified at the transcript-level using the pseudo-aligner salmon v1.10.1 (RRID:SCR_017036⁵³;) against the *A. ocellaris* reference transcriptome, using the genome as a decoy (decoy-aware pseudo-alignment; assembly ASM2253959v1³⁰), as per documentation, and using flags --validateMappings --seqBias --gcBias. The average mapping rate was above 86% of total reads. Salmon output transcript-based quantification files (quant.sf) were imported in RStudio (RRID:SCR_000432; Posit team, 2023) and summarized at the gene level using the tximport function from the tximport package (RRID:SCR_016752⁵⁴), referencing the gene models of the *A. ocellaris* reference genome assembly ASM2253959v1. The counts matrix was obtained by re-calculating counts through the flag countsFromAbundance = "lengthScaledTPM". Gene metadata (names, descriptions) were loaded from a custom-curated reference file based on the integration of Ensembl (still based on assembly AmpOce1.0) and NCBI annotations. Counts were processed as a DGEobject (edgeR package, RRID:SCR_012802⁴⁶⁻⁴⁸;) and differences in library size were taken into account by obtaining counts per million (CPM) values to allow a comparable threshold to filter out of lowly expressed genes. Here, we only maintained genes for which at least 10 counts could be detected (arbitrary) in at least 2 or 3 samples.

Heatmap visualizations were computed as described above with the following additional step: count data was corrected for latent sources of variation not related to pigment type, tissue of origin, or anemonefish strain, using the removeBatchEffect function from the limma package (RRID:SCR_010943⁵⁵;) and as identified through the svaseq function from the sva package (RRID:SCR_012836⁵⁶).

Xenopus oocyte experiments

Plasmid construction. Tissue of juvenile fish was homogenized by mechanical agitation in a vibrating bead mill (TissueLyser II, Qiagen; 3 min, 30 Hz, room temperature). Homogenized sample lysates were stored at -80°C overnight for RNA extraction. Total RNA was extracted using TRIzol Reagent Trizol (Merck/Sigma-Aldrich). Sample RNA and d(T)23VN (ProtoScript[®] II First Strand cDNA Synthesis Kit, NEB) were denatured for 5 min at 65°C , spun in briefly and kept on ice. Manufacturer's recommendations for ProtoScript II were followed to synthesize cDNA, which was used for subsequent PCR. PCR was performed using a Biometra Tone, with 10X KOD Plus Neo Buffer, 2 mM each dNTPs, 25 mM MgSO₄, KOD-Plus-Neo Polymerase, 100 ng template, and 50 μ M primer sets to a total volume of 50 μ L. DNA fragments were electrophoresed on agarose gels, before being purified and ligated into the Zero Blunt TOPO PCR Cloning vector (Invitrogen). The resulting plasmids were used to transform *Escherichia coli* DH5 α following standard protocols.

cRNA preparation. The cDNA fragments of *A. ocellaris* connexins were amplified with KOD-FX polymerase (TOYOBO). The amplified fragments were digested with EcoRI and NotI and ligated into the pGEM-HeFX plasmid. The resulting plasmids were linearized using appropriate restriction enzymes and then used as templates for in vitro cRNA synthesis with mMESSAGE mMACHINE T7 Transcription Kit (Invitrogen), according to the manufacturer's protocol.

For the zebrafish *cx41.8* E42K mutant, the G124A DNA substitution was introduced into the previously used pGEM-HeFx-zfcx41.8 plasmid¹⁷ by PCR with KOD-Fx polymerase. The resulting PCR product was used for transformation of *E. coli*. After selection, plasmids were isolated from colonies, and those containing the confirmed G124A DNA substitution were used as templates for in vitro cRNA synthesis.

Preparation of Xenopus oocytes. Whole cell voltage clamp recording with *Xenopus* oocytes were performed as described¹⁷. For

electrophysiological analysis of heterotypic gap junctions, oocytes injected with different connexin cRNA were paired after vitelline membrane removal.

Transjunctional (gap junction) current recording. Transjunctional currents were measured using the dual whole-cell voltage clamp technique with two iTEV90 multielectrode clamp amplifiers. Current and voltage electrodes were prepared with a micropipette puller P-1000 (Sutter Instrument) to obtain a resistance of 0.5–1.0 MΩ. The pipette was filled with solution containing 3 M KCl, 10 mM EGTA, and 10 mM HEPES (pH 7.4). Both cells were initially clamped at –40 mV and one cell was then subjected to 3-s voltage steps from –140 to +60 mV in 20 mV increments. Currents detected in the second oocyte were recorded and the current values at the end of the steady state of –100 mV were compared.

Zebrafish experiments

Fish stocks. The semi-dominant zebrafish allele *gja5b*^{st710} was obtained in an ethynitrosourea F3 forward genetic screen⁵⁷ and maintained subsequently in the AB* background. The mutant was mapped by association with variants identified by whole-genome resequencing of pooled genomic DNA of wild-type and mutant individuals^{21,58}, with confirmation of mutant lesion by Sanger sequencing. Subsequent phenotypic analyses of *gja5b*^{st710} used fish maintained in AB*.

Plasmid construction. *defb1:gja5b*^{WT}-*DrIRES-nEos*, *defb1:gja5b*^{st710}-*DrIRES-nEos*, *mitfa:gja5b*^{WT}-*DrIRES-nEos* and *mitfa:gja5b*^{st710}-*DrIRES-nEos* plasmids were assembled using Gibson Assembly Master Mix (NEB E2611) according to manufacturer's protocol. Plasmids containing regulatory sequences of *mitfa* (melanophore and xanthophore lineage) and *defb1* (iridophore and melanoleucophore lineages) have been described^{20,21}. Constructs used destination plasmid Tol2pA2 from the Tol2kit as backbone⁵⁹; coding sequences of *gja5b*^{wt} or *gja5b*^{st710} were cloned from genomic DNA.

Microinjection. Plasmids were injected at one-cell stage with *tol2* mRNA at 25 ng per embryo. Injected embryos were reared in accordance with the recommendations in the Guide for the Care and Use of Laboratory Animals of the National Institutes of Health and approved institutional Animal Care and Use Committee (ACUC) protocol (#4170) of the University of Virginia.

Imaging and documentation. Fish were anesthetized in MS222 (Syndel USA) prior to imaging. In some microscopic images, fish older than 5 dpf were anesthetized and treated with 1 mg/mL epinephrine (Sigma-Aldrich) to contract pigment granules. Whole adult fish images were acquired using a Nikon D810 full-frame DSLR camera with a 105 mm MicroNikkor macro lens. All other bright-field images were collected with Zeiss AxioZoom stereomicroscope, or Zeiss AxioObserver inverted microscope equipped with Zeiss AxioCam color cameras using ZEN Blue software. For developmental time series of *gja5b*^{st710} mutants and wild-type siblings, fish were imaged daily through stages of adult pattern formation as described^{60,61}, with melanin contracted to cell centers by pre-treatment with epinephrine. For easier visualization of lightly melanized cells in schematics, brightfield color images were binarized and pseudocolored and boundaries of individual melanin spots representing individual cells were enlarged uniformly by processing in Adobe Photoshop. Other images were color balanced and adjusted for display levels in Adobe Photoshop. Quantification of pattern variation in transgenic zebrafish fish followed the same methods as used for anemonefish, described above.

Gap junction gene expression in zebrafish. Re-analyses of single nuclear gene expression data from⁶² for dot-plot of gap gene transcript

abundance in pigment cell and other cells during adult pattern formation used built-in functions of Monocle 3⁶³.

Edwards-Wilkinson modeling

Matlab R2020b was used as programming language.

Bar profile extraction and preprocessing. From each image (representing 10 wild-type and 10 *Snowflake* individuals), the dorsal-ventral bar was segmented. For each row $i = 1, \dots, R$ of the grayscale mask were located the leading-edge coordinate x_i and computed the local height

$$h_i = \frac{1}{\sum_j I_{i,j}} \sum_j I_{i,j} \times \Delta y,$$

where $I_{i,j}$ is the grayscale intensity at pixel (i, j) and Δy is the calibrated pixel height. Each profile was then rotated and vertically shifted so that $h(0) = h(L) = 0$, where L is the total physical bar length.

Height-difference variance. For each profile a band pass filter was applied to isolate the modes in which the power spectrum followed k^{-2} . The filtered spectrum was transformed back into real space, and the height-difference variance was computed

$$V(\Delta x) = \left\langle [h(x + \Delta x) - h(x)]^2 \right\rangle_x$$

Analytical prediction and estimation of s^2/D . The one-dimensional Edwards-Wilkinson (EW) model predicts the exact height-difference variance is

$$V_{int}(\Delta x) = \frac{2\sigma^2}{\pi D} \int_{k_{min}}^{k_{max}} \frac{1 - \cos(k\Delta x)}{k^2} dk,$$

where s^2/D is the noise-to-surface-tension ratio. To estimate s^2/D from data, the power spectrum was computed (Fig. S6A–D)

$$P(k) = \frac{1}{N} |H(k)|^2, H(k) = \sum_{j=1}^N h(x_j) e^{-ikx_j},$$

and fitted in the band $k_{min} \leq k \leq k_{max}$ to the scaling law

$$P(k) \sim \frac{\sigma^2}{D} \frac{1}{k^2}$$

From this an empirical value of s^2/D was obtained.

Statistical analysis. All variance curves were computed for each of $n = 10$. Means and standard errors are reported.

Reporting summary

Further information on research design is available in the Nature Portfolio Reporting Summary linked to this article.

Data availability

The sequencing data (raw reads of bulk DNA seq and RNAseq) generated in this study have been deposited in the NCBI database under NCBI BioProject accession number [PRJNA1168256](https://www.ncbi.nlm.nih.gov/bioproject/PRJNA1168256). Images generated in this study have been deposited at Zenodo 10.5281/zenodo.16892159 (<https://zenodo.org/records/16892159>). Source data are provided with this paper.

Code availability

Count matrices and codes generated in this study have been deposited at Zenodo 10.5281/zenodo.16892159 (<https://zenodo.org/records/16892159>).

References

1. Marshall, N. J., Cortesi, F., de Busserolles, F., Siebeck, U. E. & Cheney, K. L. Colours and colour vision in reef fishes: Past, present and future research directions. *J. Fish. Biol.* **95**, 5–38 (2019).
2. Patterson, L. B. & Parichy, D. M. Zebrafish pigment pattern formation: Insights into the development and evolution of adult form. *Annu. Rev. Genet.* **53**, 505–530 (2019).
3. Kondo, S., Watanabe, M. & Miyazawa, S. Studies of Turing pattern formation in zebrafish skin. *Philos. Trans. R. Soc. Lond. A: Math., Phys. Engineering Sci.* **379**, 20200274 (2021).
4. Miyazawa, S. Pattern blending enriches the diversity of animal colorations. *Sci. Adv.* **6**, eabb9107 (2020).
5. Watanabe, M. et al. Spot pattern of leopard Danio is caused by mutation in the zebrafish connexin41. 8 gene. *EMBO Rep.* **7**, 893–897 (2006).
6. Irion, U. et al. Gap junctions composed of connexins 41.8 and 39.4 are essential for colour pattern formation in zebrafish. *Elife* **3**, e05125 (2014).
7. Salis, P., Lorin, T., Laudet, V. & Frédérick, B. Magic traits in magic fish: understanding color pattern evolution using reef fish. *Trends Genet.* **35**, 265–278 (2019).
8. Parichy, D. M. Evolution of pigment cells and patterns: recent insights from teleost fishes. *Curr. Opin. Genet. Dev.* **69**, 88–96 (2021).
9. Salis, P. et al. Ontogenetic and phylogenetic simplification during white stripe evolution in clownfishes. *BMC Biol.* **16**, 90 (2018).
10. Miyake, M. et al. Anemonefish Chromatophore Distribution and Organization Revealed by TEM Studies. *Zool. Sci.* **42**, 389–399 (2025).
11. Salis, P. et al. Developmental and comparative transcriptomic identification of iridophore contribution to white barring in clownfish. *Pigment Cell Melanoma Res.* **32**, 391–402 (2019).
12. Klann, M. et al. Variation on a theme: pigmentation variants and mutants of anemonefish. *EvoDevo* **12**, 8 (2021).
13. Betancur-R, R. et al. Phylogenetic classification of bony fishes. *BMC Evolut. Biol.* **17**, 162 (2017).
14. Watanabe, M. & Kondo, S. Changing clothes easily: connexin41. 8 regulates skin pattern variation. *Pigment Cell Melanoma Res.* **25**, 326–330 (2012).
15. Musa, H. & Veenstra, R. D. Voltage-dependent blockade of connexin40 gap junctions by spermine. *Biophysical J.* **84**, 205–219 (2003).
16. Watanabe, M. Gap junction in the teleost fish lineage: duplicated connexins may contribute to skin pattern formation and body shape determination. *Front. Cell Dev. Biol.* **5**, 13 (2017).
17. Watanabe, M., Sawada, R., Aramaki, T., Skerrett, I. M. & Kondo, S. The Physiological Characterization of Connexin41.8 and Connexin39.4, Which Are Involved in the Striped Pattern Formation of Zebrafish. *J. Biol. Chem.* **291**, 1053–1063 (2016).
18. Usui, Y., Aramaki, T., Kondo, S. & Watanabe, M. The minimal gap-junction network among melanophores and xanthophores required for stripe pattern formation in zebrafish. *Development* **146**, dev181065 (2019).
19. Maderspacher, F. C. Nüsslein-Volhard, Formation of the adult pigment pattern in zebrafish requires leopard and obelix dependent cell interactions. *Development* **15**, 3447–3457 (2003).
20. Huang, D. et al. Agouti and BMP signaling drive a naturally occurring fate conversion of melanophores to leucophores in zebrafish. *Proc. Natl. Acad. Sci.* **122**, e2424180122 (2025).
21. Korzeniowski, K. G. et al. Dominant Negative Mitf Allele Impacts Melanophore and Xanthophore Development and Reveals Collaborative Interactions With Tfec in Zebrafish Chromatophore Lineages. *Pigment Cell Melanoma Res.* **38**, e70009 (2025).
22. Edwards, S. F. & Wilkinson, D. R. The surface statistics of a granular aggregate. *Proc. R. Soc. A: Math., Phys. Eng. Sci.* **381**, 17–31 (1982).
23. Owen, J. P., Kelsh, R. N. & Yates, C. A. A quantitative modelling approach to zebrafish pigment pattern formation. *eLife* **9**, e52998 (2020).
24. Djurdjević, I., Furmanek, T., Miyazawa, S. & Sušnik Bajec, S. Comparative transcriptome analysis of trout skin pigment cells. *BMC Genomics* **20**, 359 (2019).
25. Li, J. et al. Cis-acting mutation affecting GJA5 transcription is underlying the Melanotic within-feather pigmentation pattern in chickens. *Proc. Natl. Acad. Sci.* **118**, e2109363118 (2021).
26. Inaba, M. et al. Instructive role of melanocytes during pigment pattern formation of the avian skin. *Proc. Natl. Acad. Sci.* **116**, 6884–6890 (2019).
27. Salazar-Ciudad, I. & Cano-Fernández, H. Evo-devo beyond development: Generalizing evo-devo to all levels of the phenotypic evolution. *Bioassays* **45**, e2200205 (2023).
28. McKenna, A. et al. The Genome Analysis Toolkit: a MapReduce framework for analyzing next-generation DNA sequencing data. *Genome Res.* **20**, 1297–1303 (2010).
29. Bolger, A. M., Lohse, M. & Usadel, B. Trimmomatic: a flexible trimmer for Illumina sequence data. *Bioinformatics* **30**, 2114–2120 (2014).
30. Ryu, T. et al. A chromosome-scale genome assembly of the false clownfish, *Amphiprion ocellaris*. *G3 Genes|Genomes|Genet.* **12**, jkac074 (2022).
31. Langmead, B. & Salzberg, S. L. Fast gapped-read alignment with Bowtie 2. *Nat. Methods* **9**, 357–359 (2012).
32. M. Vasimuddin, S. Misra, H. Li, S. Aluru, in *2019 IEEE International Parallel and Distributed Processing Symposium (IPDPS)*. (2019), pp. 314–324.
33. Shumate, A. & Salzberg, S. L. Liftoff: accurate mapping of gene annotations. *Bioinformatics* **37**, 1639–1643 (2021).
34. Cingolani, P. et al. A program for annotating and predicting the effects of single nucleotide polymorphisms, SnpEff. *Fly. (Austin)* **6**, 80–92 (2012).
35. Mikalsen, S., Tausen, M. & í Kongsstovu, S. Phylogeny of teleost connexins reveals highly inconsistent intra- and interspecies use of nomenclature and misassemblies in recent teleost chromosome assemblies. *BMC Genomics* **21**, 223 (2020).
36. Roux, N. et al. A star is born again: Methods for larval rearing of an emerging model organism, the False Clownfish *Amphiprion ocellaris*. *J. Exp. Zool. Part B: Mol. Dev. Evol.* **336**, 376–385 (2021).
37. Murakami, Y., Futamata, R., Horibe, T., Ueda, K. & Kinoshita, M. CRISPR/Cas9 nickase-mediated efficient and seamless knock-in of lethal genes in the medaka fish *Oryzias latipes*. *Dev., Growth Differ.* **62**, 554–567 (2020).
38. Danecek, P. et al. Twelve years of SAMtools and BCFtools. *Giga-science* **10**, giab008 (2021).
39. Robinson, J. T. et al. Integrative genomics viewer. *Nat. Biotechnol.* **29**, 24–26 (2011).
40. Thorvaldsdóttir, H., Robinson, J. T. & Mesirov, J. P. Integrative Genomics Viewer (IGV): high-performance genomics data visualization and exploration. *Brief. Bioinform* **14**, 178–192 (2013).
41. Yamanaka, S., Okada, Y., Furuta, T. & Kinoshita, M. Establishment of culture and microinjection methods for false clownfish embryos without parental care. *Dev., Growth Differ.* **63**, 459–466 (2021).
42. Urasaki, A., Morvan, G. & Kawakami, K. Functional dissection of the Tol2 transposable element identified the minimal cis-sequence and a highly repetitive sequence in the subterminal region essential for transposition. *Genetics* **174**, 639–649 (2006).
43. Kawakami, K. et al. A transposon-mediated gene trap approach identifies developmentally regulated genes in zebrafish. *Dev. Cell* **7**, 133–144 (2004).
44. Roux, N. et al. Staging and normal table of postembryonic development of the clownfish (*Amphiprion ocellaris*). *Dev. Dyn.* **248**, 545–568 (2019).

45. Bray, N. L., Pimentel, H., Melsted, P. & Pachter, L. Near-optimal probabilistic RNA-seq quantification. *Nat. Biotechnol.* **34**, 525–527 (2016).
46. Robinson, M. D., McCarthy, D. J. & Smyth, G. K. edgeR: a Bioconductor package for differential expression analysis of digital gene expression data. *Bioinformatics* **26**, 139–140 (2010).
47. McCarthy, D. J., Chen, Y. & Smyth, G. K. Differential expression analysis of multifactor RNA-Seq experiments with respect to biological variation. *Nucleic Acids Res.* **40**, 4288–4297 (2012).
48. Chen, Y., Chen, L., Lun, A. T. L., Baldoni, P. L. & Smyth, G. K. edgeR v4: powerful differential analysis of sequencing data with expanded functionality and improved support for small counts and larger datasets. *Nucleic Acids Res.* **53**, gkaf018 (2025).
49. Love, M. I., Huber, W. & Anders, S. Moderated estimation of fold change and dispersion for RNA-seq data with DESeq2. *Genome Biol.* **15**, 550 (2014).
50. Gu, Z. Complex heatmap visualization. *iMeta* **1**, e43 (2022).
51. Gu, Z., Eils, R. & Schlesner, M. Complex heatmaps reveal patterns and correlations in multidimensional genomic data. *Bioinformatics* **32**, 2847–2849 (2016).
52. S. Andrews. (online, 2010).
53. Patro, R., Duggal, G., Love, M. I., Iziray, R. A. & Kingsford, C. Salmon provides fast and bias-aware quantification of transcript expression. *Nat. Methods* **14**, 417–419 (2017).
54. Sonesson, C., Love, M. I. & Robinson, M. D. Differential analyses for RNA-seq: transcript-level estimates improve gene-level inferences. *F1000Research* **30**, 1521 (2015).
55. Ritchie, M. E. et al. limma powers differential expression analyses for RNA-sequencing and microarray studies. *Nucleic Acids Res.* **43**, e47 (2015).
56. Leek, J. T., Johnson, W. E., Parker, H. S., Jaffe, A. E. & Storey, J. D. The sva package for removing batch effects and other unwanted variation in high-throughput experiments. *Bioinformatics* **28**, 882–883 (2012).
57. Solnica-Krezel, L., Schier, A. F. & Driever, W. Efficient recovery of ENU-induced mutations from the zebrafish germline. *Genetics* **136**, 1401–1420 (1994).
58. Henke, K. et al. Genetic Screen for Postembryonic Development in the Zebrafish (*Danio rerio*): Dominant Mutations Affecting Adult Form. *Genetics* **207**, 609–623 (2017).
59. Kwan, K. M. et al. The Tol2kit: a multisite gateway-based construction kit for Tol2 transposon transgenesis constructs. *Dev. Dyn.* **236**, 3088–3099 (2007).
60. McCluskey, B. M., Uji, S., Mancusi, J. L., Postlethwait, J. H. & Parichy, D. M. A complex genetic architecture in zebrafish relatives *Danio quagga* and *D. kyathit* underlies development of stripes and spots. *PLoS Genet.* **17**, e1009364 (2021).
61. Eom, D. S. et al. Melanophore migration and survival during zebrafish adult pigment stripe development require the immunoglobulin superfamily adhesion molecule Igslf11. *PLoS Genet.* **8**, e1002899 (2012).
62. Aman, A. J. et al. Transcriptomic profiling of tissue environments critical for post-embryonic patterning and morphogenesis of zebrafish skin. *Elife* **12**, RP86670 (2023).
63. Cao, J. et al. The single-cell transcriptional landscape of mammalian organogenesis. *Nature* **566**, 496–502 (2019).

Acknowledgements

We thank the OIST sequencing center as well as the imaging section. We are grateful for the support of our husbandry teams at OIST and Academia Sinica, as well as the Mutualized Aquariology Service at the Oceanological Observatory of Banyuls-sur-Mer, France. We thank the High Throughput Genomics Core of the Biodiversity Research Center at Academia Sinica for performing the NGS experiments. The core facility is

funded by Academia Sinica Core Facility and Innovative Instrument Project (AS-CFII-108-114). We specifically thank Dr. Mei-Yeh Lu, Mr. Kuan-Ying Li, and Ms. Pei-Lin Chao for their efforts and assistance. We thank Simon de Bernard and Laurent Buffat from Altrabio for the initial bioinformatic analysis of the genome resequencing data. We are very grateful to Shigeru Kondo for support and helpful discussion during the early stages of this work. This work has been funded by the following sources: JSPS Grant-in-Aid for Scientific Research B 22H02678 (VL, MKi), JSPS Grant-in-Aid for Scientific Research C 24K09472 (MW), OIST KICKS Program for Research Scholarship Fund (VL), Grand Challenge Project AS-GC-111-L06 (VL), National Institutes of Health grant R35 GM122471 (DMP), National Institutes of Health grant R35 GM118179 (LS-K), and Agence Nationale de la Recherche, project SENSO ANR19-CE14-0010 (LB).

Author contributions

[Marleen Klann (MKI), Masato Kinoshita (MKi)]. Conceptualization: M.K.L., M.Ki., D.M.P., V.L., Data curation: M.H., S.D.V., R.R. Formal analysis: M.H., S.D.V., E.G., B.M.M., R.R., S.P., D.M.P. Methodology: R.R., S.P., M.Ki. Resources: L.S-K., M.Ki. Investigation: M.K.L., S.M., S.H.L., S.D.V., H.W.H., B.M.M., R.R., M.W., Y.L., L.B., M.Ki., D.M.P. Methodology: R.R., S.P. Validation: M.Ki. Visualization: M.K.L., R.R., D.M.P. Funding acquisition: V.L., D.M.P., L.S-K., M.Ki., M.W., L.B. Supervision: D.M.P., M.Ki., V.L. Writing – original draft: M.K.L., R.R., S.P., M.W., M.Ki., D.M.P., V.L. Writing – review & editing: M.K.L., E.G., S.D.V., M.W., L.B., S.P., M.Ki., D.M.P., V.L.

Competing interests

The authors declare no competing interests.

Additional information

Supplementary information The online version contains supplementary material available at <https://doi.org/10.1038/s41467-026-69524-8>.

Correspondence and requests for materials should be addressed to David M. Parichy, Masato Kinoshita or Vincent Laudet.

Peer review information *Nature Communications* thanks Claudius Kratochwil and the other, anonymous, reviewer(s) for their contribution to the peer review of this work. A peer review file is available.

Reprints and permissions information is available at <http://www.nature.com/reprints>

Publisher's note Springer Nature remains neutral with regard to jurisdictional claims in published maps and institutional affiliations.

Open Access This article is licensed under a Creative Commons Attribution-NonCommercial-NoDerivatives 4.0 International License, which permits any non-commercial use, sharing, distribution and reproduction in any medium or format, as long as you give appropriate credit to the original author(s) and the source, provide a link to the Creative Commons licence, and indicate if you modified the licensed material. You do not have permission under this licence to share adapted material derived from this article or parts of it. The images or other third party material in this article are included in the article's Creative Commons licence, unless indicated otherwise in a credit line to the material. If material is not included in the article's Creative Commons licence and your intended use is not permitted by statutory regulation or exceeds the permitted use, you will need to obtain permission directly from the copyright holder. To view a copy of this licence, visit <http://creativecommons.org/licenses/by-nc-nd/4.0/>.

© The Author(s) 2026

¹Marine Eco-Evo-Devo Unit, Okinawa Institute of Science and Technology, Okinawa, Japan. ²Marine Research Station, Institute of Cellular and Organismic Biology, Academia Sinica, Yilan, Taiwan. ³Biological Complexity Unit, Okinawa Institute of Science and Technology, Okinawa, Japan. ⁴Graduate School of Frontier Biosciences, Osaka University, Osaka, Japan. ⁵Department of Biology, University of Virginia, Charlottesville, VA, USA. ⁶Department of Developmental Biology, Washington University School of Medicine, St. Louis, MO, USA. ⁷CNRS IRL 2028 “Eco-Evo-Devo of Coral Reef Fish Life Cycle” (EARLY), Okinawa, Japan. ⁸Sorbonne Université, CNRS, Biologie Intégrative des Organismes Marins, BIOM, Observatoire Océanologique, Banyuls-sur-Mer, France. ⁹Division of Applied Bioscience, Graduate School of Agriculture, Kyoto University, Kyoto, Japan. ¹⁰Present address: Cellular and Structural Physiology Institute/Graduate School of Pharmaceutical Sciences, Nagoya University, Aichi, Japan. ¹¹These authors contributed equally: David M. Parichy, Masato Kinoshita, Vincent Laudet. ✉ e-mail: dparichy@virginia.edu; kinoshita.masato.4e@kyoto-u.ac.jp; vincent.laudet@oist.jp